Modeling Earth Systems and Environment (2024) 10:2375–2392
https://doi.org/10.1007/s40808-023-01906-z

ORIGINAL ARTICLE

Advanced FELA-ANN framework for developing 3D failure envelopes for strip foundations on anisotropic clays

Duy Tan Tran[1] · Minh Nhat Tran[2,3] · Van Qui Lai[2,3] · Suraparb Keawsawasvong[1]

Received: 20 September 2023 / Accepted: 6 November 2023 / Published online: 16 December 2023
© The Author(s), under exclusive licence to Springer Nature Switzerland AG 2023

Abstract

A finite element limit analysis (FELA) combined with a machine learning technique is adopted to determine failure envelopes of a strip footing resting on anisotropic soil under combined loadings (*V, H, M*). Based on numerical results from 2D FELA, the parametric studies on the failure envelopes in the 2D space (*H, M*) and 3D space (*V, H, M*) considering the effect of anisotropic behaviors of clays and interface interaction between soil and structure, are investigated. Additionally, the failure mechanisms of the investigated strip footings are also illustrated. These results can enhance the understating of practical engineering for designing a strip footing resting on anisotropic soil under combined loadings (*V, H, M*). In the later part, an artificial neural network (ANN) is adopted to propose the correlation equation between input parameters and their corresponding outputs using the data from FELA. Based on the developed ANN model, building the failure envelopes of strip footing subjected to general load (*V, H, M*) becomes quicker than the traditional methods. For more detail, the careful explanation for applying ANN results is presented through the design example. It can be a valuable procedure for practical engineers to establish the failure envelope of a footing on anisotropic clay under combined loading (*V, H, M*).

Keywords General loading · Envelope · Footing · FELA · ANN

Introduction

In geotechnical engineering science, considering general loading is essential when designing shallow foundations for offshore structures since the significant lateral forces generated by wind and waves commonly occur. Consequently, the footings of offshore structures often experience general load consisting of vertical load (*V*), horizontal load (*H*), and bending moment (*M*). Various numerical and experimental studies have explored the behavior of different foundation types subjected to general loading in clay. These studies include the works of Bransby and Randolph (1998), Bransby and Yun (2009), Martin (1994), Martin and Houlsby (2000), Gourvenec and Randolph (2003), Gourvenec (2008), Gourvenec and Barnett (2011), Taiebat and Carter (2000), Yun and Bransby (2007), and Bolton and Lau (1993). Generally, the combined loading problems were based on the traditional bearing capacity design method, as proposed by Brinch Hansen (1970), Meyerhof (1953), Vesic (1975), and Das and Larbi-Cherif (1983). In detail, these approaches adjusted a footing's bearing capacity for eccentric and inclined loads.

An additional alternative method, which provides increased accuracy, involves explicitly expressing the capacity of a foundation under various loading conditions, as expressed by a 3D failure envelope in a (*V-H-M*) space. This 3D failure envelope is illustrated as a 3D surface, where those positions outside the surface represent the situation that footings lead to failure, while those inside the surface mean that the footing does not fail and is deemed safe. The methodology of this failure envelope was initially proposed by Roscoe and Schofield (1957), who presented an extensive application of the failure envelope in the field of bearing capacity problems. Numerous studies have explored

✉ Suraparb Keawsawasvong
ksurapar@engr.tu.ac.th

[1] Research Unit in Sciences and Innovative Technologies for Civil Engineering Infrastructures, Department of Civil Engineering, Thammasat School of Engineering, Thammasat University, Pathumthani 12120, Thailand

[2] Faculty of Civil Engineering, Ho Chi Minh City University of Technology (HCMUT), 268 Ly Thuong Kiet Street, District 10, Ho Chi Minh City, Vietnam

[3] Vietnam National University Ho Chi Minh City (VNU-HCM), Linh Trung Ward, Thu Duc District, Ho Chi Minh City, Vietnam

the utility of this methodology, including previous works by Butterfield and Ticof (1979), Butterfield and Gottardi (1994), Feng et al. (2014), Martin and Houlsby (2001), Gourvenec (2007), Mana et al. (2013), Nova and Montrasio (1991), Ukritchon et al. (1998), Vulpe et al. (2013), Zhang et al. (2011), and Ibrahim et al. (2022).

It is worth noting that soils typically exhibit various levels of strength anisotropy, as highlighted in previous studies by Davis and Christian (1971), Ladd and Degroot (2003), Law (1978), Pan and Dias (2016), Reddy and Rao (1981), Su et al. (1998), Ukritchon et al. (2003), Kumar and Ghosh (2007), and Yang and Du (2016). These investigations have explored the significant impact of the anisotropic characteristics of natural clays on foundation stability. The existing studies primarily focus on the foundations on isotropic clays that adhere to the Mohr–Coulomb or Tresca failure criterion. However, they do not take into account the anisotropy of clays. Additionally, there has been no literature proposing solutions for determining the failure envelopes of strip foundations under general loading *(V, H, M)* on anisotropic clays.

This study aims to analyze the capacity of strip footings on anisotropic clays under general *V-H-M* loading. The 3D failure envelope in (*V-H-M*) space and the 2D failure envelope in (*H-M*) spacing considering the effect of the anisotropic behavior of clay and interface interaction between soil and footing are investigated. According to the structure of this study, the parametric analysis is first derived from 2D finite element limit analyses (FELA) to consider the effect of the anisotropic behavior of clay and the soil-structure interface interaction on the bearing capacity of strip footings under general *V-H-M* loading. Then, the Artificial Neural Network (ANN) models are adopted in this study to depict a correlation that relates the input variables to the corresponding output outcomes. Based on the analysis of parametric study results, the proposed correlation equation from the optimal ANN model can assist engineers in real applications by enabling them to build a failure envelope of strip footing under combined loading (*V, H, M*). It can be helpful for practitioners to check the capacity of strip foundations subjected to combined loads (*V, H, M*).

Problem statement

Problem definition

The challenge of analyzing a rigid strip footing placed on anisotropic clay subjected to various loads is illustrated in Fig. 1. The width of a strip footing is denoted as (*B*). The rigid plate elements simulate the strip foundation by assuming the footing to be highly rigid and incapable of failure. As a result, the rigid footing effectively transfers all loads to the ground. The strip footing is subjected to various loads involving vertical force (*V*), horizontal force (*H*), and bending moment (*M*). It is important to emphasize that the positive orientation is assigned to the vertical load in the compression condition (vertical load applied downward to the footing). Tensile forces in the vertical direction are not considered in this study, where only compressive vertical forces are considered. The clay profile underlying the strip footing is assumed to be anisotropic and weightless.

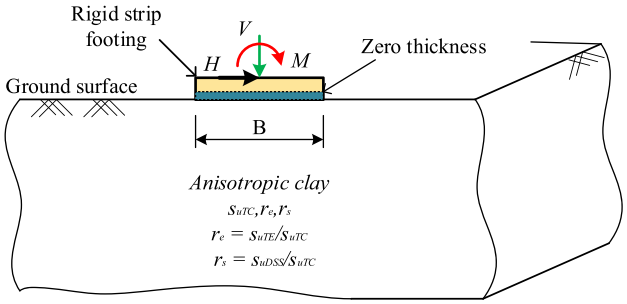

Fig. 1 Problem definition for obtaining 3D failure envelope of a strip footing on anisotropic clay

The numerical models are simulated following two cases of soil-structure interfaces, including "full-tension" condition (in the case of no separation between soil and footing) and "no-tension" condition (in the case of separation allowed to occur). Note that "zero-thickness" interface elements are applied to connect footing and soil (see Fig. 1). For the no-tension condition, the tension cut-off function for the failure criterion is activated. According to this function, the tensile stresses are not allowed to take place at the interface, so that the separation may happen underneath the footing. Conversely, the tension cut-off function has been deactivated to simulate the full-tension condition accurately.

AUS failure criterion

In this investigation, the Anisotropic Undrained Shear (AUS) failure criterion (Krabbenhoft et al. 2019) is utilized to develop the criterion for covering the failure behavior of anisotropic clays. The soil strength requirement for the AUS model is based on three distinct anisotropic undrained shear strengths, which can be acquired through triaxial compression (s_{uTC}), triaxial extension (s_{uTE}), and direct simple shear (s_{uDSS}) tests. In order to emphasize the variability in undrained strength across various directions, two anisotropic strength ratios, denoted as r_e and r_s, are introduced. These ratios serve as the dimensionless input parameters in the present study, where their

expressions are described in Eqs. (1) and (2) as shown below:

$$r_e = \frac{s_{uTE}}{s_{uTC}} \tag{1}$$

and

$$r_s = \frac{s_{uDSS}}{s_{uTC}} \tag{2}$$

Krabbenhoft et al. (2019) further explained that the harmonic mean can be derived from the relationship between r_s and r_e, expressed as Eq. (3) follows:

$$r_s = \frac{2r_e}{1 + r_e} \tag{3}$$

where the variable r_e falls within the range of 0.5 to 1. As mentioned by Krabbenhoft et al. (2019), altering the value of (r_e) results in a corresponding modification of the failure surface following the AUS failure criterion, as illustrated in Fig. 2. The case of an isotropic clay can be analyzed by establishing $r_e = 1$, meaning $s_{uTC} = s_{uTE} = s_{uDSS}$, so that the AUS failure criterion can be transformed into the Tresca failure criterion. Based on Eq. (5), considering the anisotropy effect of clay can be determined through only the parameter (r_e).

Failure envelop

In this study, a 3D failure envelope in the space of *V-H-M* is adopted to express the undrained capability for the strip footing in anisotropic clay under various loading conditions. For practical application, the output results (*V-H-M)* of the 3D failure envelope are normalized following the dimensionless approach as introduced by Butterfield (1999). Combined with considering the anisotropic behavior of clay, the normalized output results (*V-H-M)* can be expressed as the function of r_e, as shown in Eq. (4):

$$\frac{V}{s_{uTC}B}, \frac{H}{s_{uTC}B}, \frac{M}{s_{uTC}B^2} = f(r_e) \tag{4}$$

where $V/s_{uTC}B$ is the non-dimensional vertical load coefficient; $H/s_{uTC}B$ is the non-dimensional horizontal load coefficient; $M/s_{uTC}B^2$ is the non-dimensional bending moment coefficient, and r_e represents the anisotropic ratio.

To build a 3D failure envelope through dimensionless variables ($V/s_{uTC}B$, $H/s_{uTC}B$, $M/s_{uTC}B^2$), the dimensionless vertical load factor, $V/s_{uTC}B$, can be broken into the ratios between the levels of vertical load mobilization (V/V_0) and $V_0/s_{uTC}B$, as shown in Eq. (5):

$$\frac{V}{s_{uTC}B} = \frac{V}{V_0} \times \frac{V_0}{s_{uTC}B} \tag{5}$$

where V_0 is the ultimate load of a strip foundation under the pure vertical loading (pure *V*) for each of the soil profiles. It is important to note that the value of $V_0/s_{uTC}B$ is first determined before carrying out the failure envelope analysis and V_0 is dependent on the (s_{uTC}, B, r_e). After obtaining the value of $V_0/s_{uTC}B$, the value of $V/s_{uTC}B$ can be calculated by multiplying with the value of V/V_0 in ranges of [0, 0.2; 0.4; 0.6; 0.8, 1]. In other words, the value of $V/s_{uTC}B$ is varied from 0 to $V_0/s_{uTC}B$. According to this change, the investigated 3D failure envelope ($V/s_{uTC}B$, $H/s_{uTC}B$, $M/s_{uTC}B^2$) is now changed to 3D failure envelope (V/V_0, $H/s_{uTC}B$, $M/s_{uTC}B^2$). This kind of 3D failure envelope (V/V_0, $H/s_{uTC}B$, $M/s_{uTC}B^2$) previously mentioned by Gottardi and Butterfield (1993), Houlsby and Puzrin (1999), Taiebat and Carter (2002), and Gourvenec and Randolph (2003).

An example of a 3D failure envelope is shown in Fig. 3, indicating a three-dimensional interaction plot within the (V/V_0, $H/s_{uTC}B$, $M/s_{uTC}B^2$) space is used to express the undrained capacity of strip footings under general loading. Each point on the surface of the 3D failure envelope corresponds to various plastic zones and failure mechanisms, encompassing a combination of failure modes, including rotations, bearing capacity, and translations. Additionally, Fig. 4 presents the contour of the 3D failure envelope corresponding to a cross-section of the vertical load ratio, V/V_0. It can be considered as a 2D failure envelope in the *M-H* space ($M/s_{uTC}B^2$, $H/s_{uTC}B$) at a specific value of V/V_0.

As illustrated in Fig. 4, two separate scenarios are analyzed for each envelope within the ($H/s_{uTC}B$, $M/s_{uTC}B^2$) space. In the first quadrant, labeled as "I" in the first portion, the lateral load and bending moment induces a footing toppling in the same direction. In another case, labeled as "II" in the second quadrant, the overturning movement happens

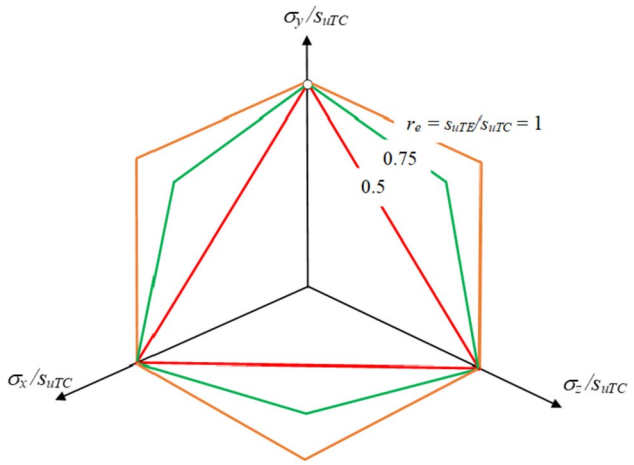

Fig. 2 The formations of the yield surfaces of the AUS model with various r_e values

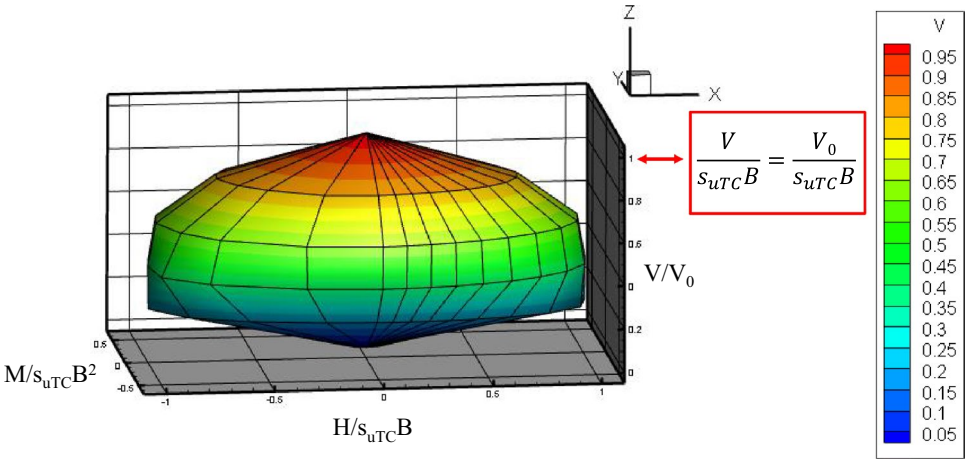

Fig. 3 3D failure envelope through three dimensionless variables (V/V_0, $H/s_{uTC}B$, $M/s_{uTC}B^2$)

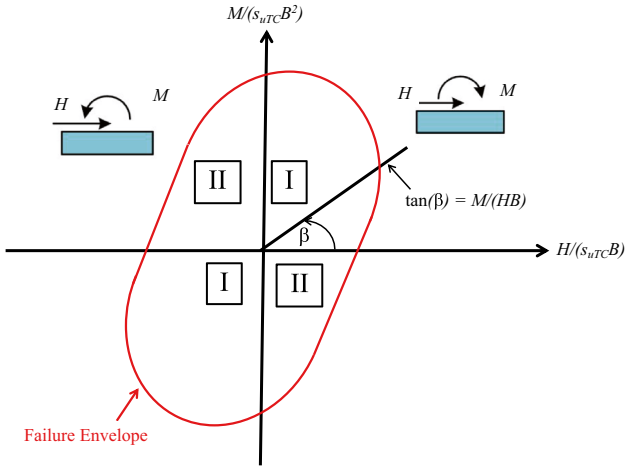

Fig. 4 Establishing the 2D failure envelope for a specified value of V/V_0

in opposite directions due to the different directions between the lateral load and bending moment, as emphasized in prior research conducted by Keawsawasvong and Ukritchon (2016). The remaining plots in the third and fourth quadrants can be derived through problem anti-symmetry, where the results in the first and the second quadrants match those in the third and fourth quadrants (see Fig. 4).

To build a 3D failure envelope (V/V_0, $H/s_{uTC}B$, $M/s_{uTC}B^2$), the 2D failure envelope ($H/s_{uTC}B$, $M/s_{uTC}B^2$) is first determined for the five cross-sections of $V/V_0 = 0$, 0.2, 0.4, 0.6, and 0.8. To define the 2D failure envelope in the $H/s_{uTC}B$—$M/s_{uTC}B^2$ space, it needs to define the proportion between horizontal load and bending moment through $\tan(\beta) = M/HB$ or $M = \tan(\beta)(HB)$. The value of β represents the angle assessed starting from the positive of the horizontal axis (refer to Fig. 4) (Salencon and Peeker 1995; Keawsawasvong and Ukritchon 2016). In this study, the value of β is selected within the ranges from 0° to 180° with the interval of 10°, serving as the loading constraint for the FELA. Note that the values of (V_o, H, and M) are determined using the FELA models.

Methodology

FELA model

The FELA technique has demonstrated a notable level of accuracy and precision in its outcomes. It offers both lower bound (LB) and upper bound (UB) solutions, resulting in an estimation of an exact value (Sloan 2013; Lai et al. 2023; Kumar et al. 2023a, b). The lower bound (LB) analysis defines soil mass as the three-node triangular element with four unknown stresses under plane strain and axisymmetric conditions. Stress discontinuities can exist along all shared edges of surrounding components (especially interfacial aspects) by modeling each triangle element with its unique nodes. The computation of LB is performed by employing the Second Order Cone Program (SOCP), which produces a stress field that satisfies the equilibrium equations at triangle elements and across stress discontinuities, stress boundary conditions, and yield criteria. The LB SOCP optimization procedure aims to optimize the ultimate pressure influenced by the unknown nodal stresses. The upper bound calculations include dividing the soil mass around the shell foundation into triangular pieces with six nodes. Each node is coupled to two unknown velocities, which account for both plane strain and axisymmetric circumstances. The unknown speeds are the same between elements close to each other and are calculated using a quadratic formula inside each component. It should be noted that velocity discontinuities can only occur in interface elements defined by soil footing interfaces. The kinematically acceptable velocity field to satisfy velocity boundary conditions and the compatibility

equations with the associated flow rule at triangular and interfacial pieces are generated by the UB computation's second-order conic programming (SOCP) formulation. The ultimate pressure (Krabbenhoft et al. 2019) is the goal of the UB SOCP optimization. UB solutions can be accomplished by utilizing the virtual work framework, which contrasts the work done by external loads with the internal energy dissipation at triangular interfacial parts.

In this study, numerical solutions of the capacity of rigid strip footings placed on anisotropic clays under combined loads are calculated utilizing the OptumG2 FELA software (Krabbenhoft et al. 2015). The typical model geometry for this problem is shown in Fig. 5. The interaction between the soil and footing is represented in the model by incorporating "no-tension" and "full-tension" conditions, which permit the underlying soil to "separate" or "not to separate" from the footing, respectively, as mentioned in the section of the problem definition. Soil elements are modeled by obeying the AUS model. Additionally, the feature of a fan mesh is activated at both corners of the footing to enhance the precision of the calculated FELA outcomes. Limiting boundary conditions for the model are assessed at a distance of 6B extended laterally from the footing center and 3B below the soil surface. The width (B) of the strip foundation was maintained at 1.0 m throughout all analyses in this research. The right and left boundaries of the domain are specified as roller supports, permitting vertical movements while restricting lateral rotations and horizontal displacements. The top ground surface is unrestricted, allowing for movement and deformation without any imposed constraints. On the other hand, the fixed support is employed to apply at the base boundary of the model, providing complete restraint against all rotations and translations.

The auto-mesh adaptive method in OptumG2 is employed to enhance the precision and dependability of numerical solutions. This technique adjusts the mesh density in specific regions based on the local solution characteristics. This auto-mesh adaptive process starts with an initial mesh configuration and employs error indicators to pinpoint areas within the domain where the solution exhibits inadequate representation. In the context of FELA, these commonly correspond to regions characterized by high shear dissipation. Once these areas are identified, the mesh is refined to enhance solution accuracy. In this study, five adaptive iterations of mesh adaptivity are employed. This study initiated this process with 5,000 elements and concluded with 10,000 elements to narrow the gap between lower and upper bounds solutions, yielding more precise and dependable outcomes.

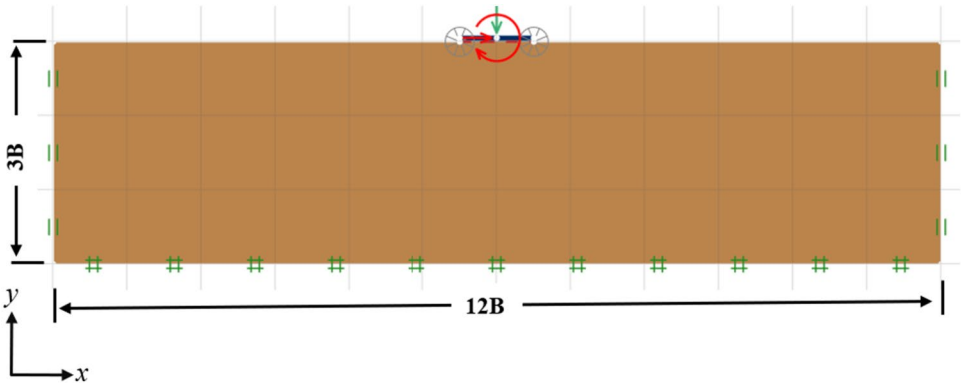

Fig. 5 FELA model of a strip footing under general loading in OptumG2

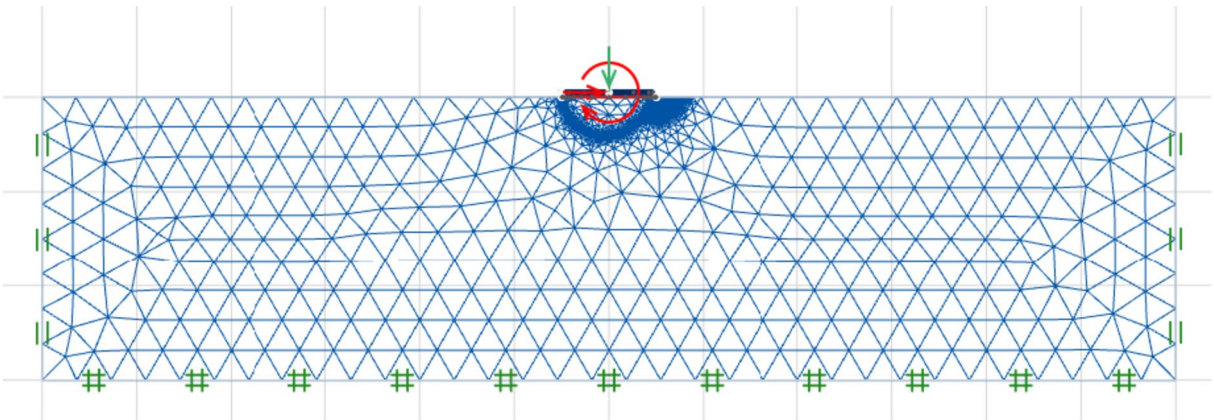

Fig. 6 An adaptive mesh pattern and boundary conditions

Increasing the number of components in the sensitive areas may improve the accuracy of the results. The meshing procedures represent the original meshes' progression toward the intended value. The solutions remain unchanged since there are enough elements and processes. An illustration of the application of the auto-mesh adaptive method for the strip footing problem is depicted in Fig. 6.

The calculation process includes two main steps. In the first step, the limit load (V_0) of strip footing, considering the anisotropic behavior of clay through a parameter (r_e), is first assessed by pure vertical applied load. In the second step, with a fixed vertical load (V) in the range [0, $0.2V_0$, $0.4V_0$, $0.6V_0$, $0.8V_0$] applied to the strip footing, the value of load combination (H, M) is determined through the multiplier technique in FELA cooperating with the value of tan(β) as mentioned in Fig. 4. In total, there are 840 analysis cases considering both "no-tension" and "full-tension" interface conditions with the ranges of (r_e, V/V_0, β), as shown in Table. 1. Based on calculation results, the 2D failure envelope ($H/s_{uTC}B$, $M/s_{uTC}B^2$) with a range of V/V_0 [0, 0.2, 0.4, 0.6, 0.8] and 3D failure envelope (V/V_0, $H/s_{uTC}B$, $M/s_{uTC}B^2$) is presented and investigated in the later part.

Machine learning model

Artificial Neural Networks (ANNs) is a complex system inspired by human brain learning. This machine learning model is how people solve and learn a particular problem. Mainly, ANNs are a layer-organized network of interconnected nodes, so-called artificial neurons, in which three types of essential layers define the architecture of neural networks and illustrate how the network transforms its input into the outcomes (Shams et al. 2020; Kapadia and Jariwala 2021; Cherif et al. 2023; Saint-Fleur et al. 2023). Figure 7 shows the architecture of a feed-forward, so-called multiple-layer network with the input, hidden, and output layers, respectively. It should be noted that each node consists of its weights and biases, which are adjusted in the training process following the Levenberg-Madquardt backpropagation algorithm (Hagan and Menhaj 1994). The backpropagation process, as shown in Fig. 8, illustrates how the network adapts by comparing its output to the desired target. Initially, the inputs transform the neural network using a transfer

Table 1 Ranges of input parameters

Variable	Selected values
V/V_0	0, 0.2, 0.4, 0.6, 0.8
r_e	0.5, 0.6, 0.7, 0.8, 0.9, 1
β	0, 15, 30, 40, 50, 60, 70, 80, 90, 100, 110, 120, 130, 140, 150, 160, 170, 180

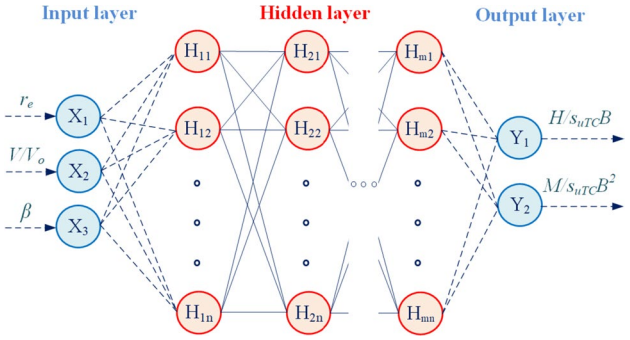

Fig. 7 The architecture of multi-layer networks

function, resulting in the output. If the output and target comparison do not meet the required criteria, the network adjusts its weights and iterates until it achieves a suitable fit. This dynamic and iterative process enables the network to learn and optimize its performance efficiently. This backpropagation has the advantage of being ten to one hundred times faster than algorithms such as Gradient Descent but requires more memory.

This paper proposes the application of artificial neural networks to determine the dimensionless horizontal load ($H/s_{uTC}B$) and bending moment factor ($M/s_{uTC}B^2$) of the strip footing on anisotropic clay under combined loading through the correlation equations. Based on these equations, the practitioners can quickly determine the 2D failure envelope ($H/s_{uTC}B$, $M/s_{uTC}B^2$) with the range of V/V_0 [0, 0.2, 0.4, 0.6, 0.8] and also the 3D failure envelope (V/V_0, $H/s_{uTC}B$, $M/s_{uTC}B^2$). The inputs to the ANN model include (r_e), the vertical load mobilization (V/V_0), and different (β) angles, respectively.

The ANN is implemented in MATLAB code (Beale et al. 2010), in which the size of input layer $Qx3$ (r_e, V/V_0, β) and the outcomes layer $Qx2$ ($H/s_{uTC}B$, $M/s_{uTC}B^2$), where Q is number 420 cases. In this study, 420 data points are randomly allocated into three sets: 70% for training, 15% for validation (to prevent overfitting), and 15% for an independent test of network performance. A two-layer feed-forward network with tan-sigmoid hidden neurons and linear output

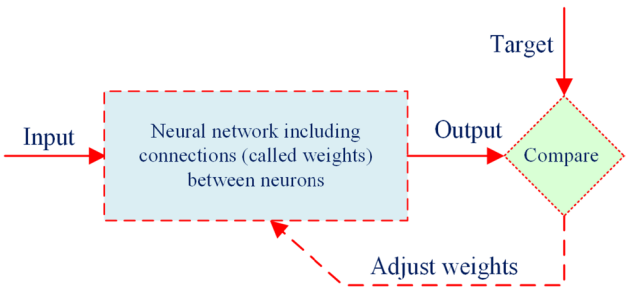

Fig. 8 The process of backpropagation

neurons is applied, and the chosen number of neurons in the hidden layer is selected and discussed in the next part. As a result, optimal weight and bias, so-called "Neural Network Constants", are generated and applied to investigate the sensitive analysis of each parameter toward their outputs (Abdollahi et al. 2021; Ahmad et al. 2022; Kumar et al. 2023a, b).

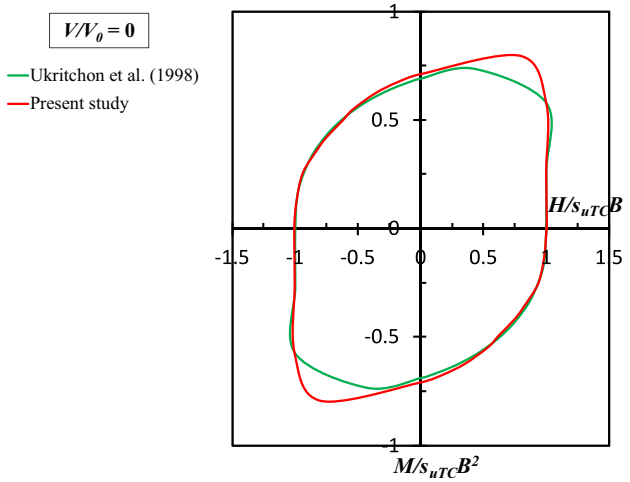

Fig. 9 A comparison of failure envelopes for strip footings on isotropic clays between the current study and the existing results from Ukritchon et al. (1998)

Results and comparisons

Verification

A comparison of failure envelopes of strip footing in clay in the ($H/s_{uTC}B$, $M/s_{uTC}B^2$) space with the cross-section of $V/V_0 = 0$ (no vertical load) between the present study and the previous numerical solutions suggested by Ukritchon et al. (1998) is presented in Fig. 9. It is noted that the case of isotropic clays is carried out by setting $r_e = 1$, meaning that the AUS failure criterion becomes the Tresca failure criterion. This figure shows that the failure envelope exhibited an elliptical shape that rotated away from the positive $H/s_{uTC}B$-axis. The current results show a favorable comparison with existing results. The current solutions are higher than the previous solutions. This difference arises because different mathematical forms of failure criteria are employed. The previous solutions utilized the Tresca model, while this study adopts the AUS model. The agreement between the previous solutions and the current results derived from the FELA analysis in the failure envelopes in (H-M) space of strip footing, is in good agreement with Ukritchon et al. (1998).

FELA results

To investigate the 3D failure envelope (V/V_0, $H/s_{uTC}B$, $M/s_{uTC}B^2$) considering the effect of anisotropic behavior of clay and soil-footing interface interaction, 2D failure envelopes ($H/s_{uTC}B$, $M/s_{uTC}B^2$) with a range of V/V_0 [0, 0.2, 0.4, 0.6, 0.8] are investigated and shown in Figs. 10, 11, 12, 13, 14 and 15. These failure envelopes in the H-M space exhibit asymmetry relative to the H-axis and M-axis, with the extent

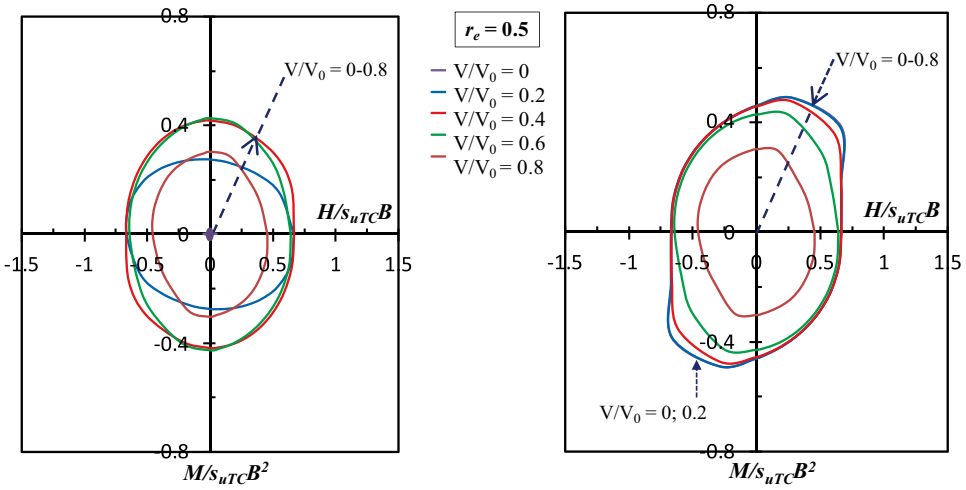

Fig. 10 Failure envelopes of strip footings with $r_e = 0.5$

(a) No tension

(b) Full tension

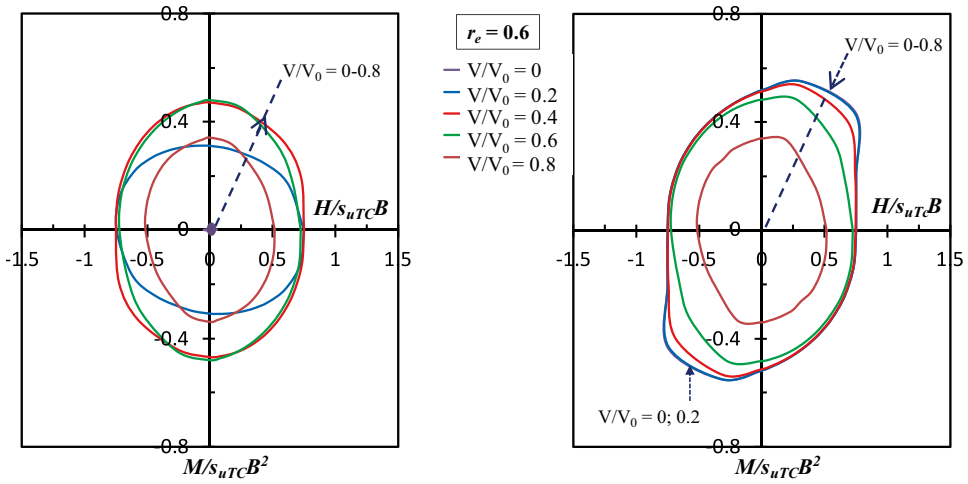

(a) No tension **(b)** Full tension

Fig. 11 Failure envelopes of strip footings with $r_e = 0.6$

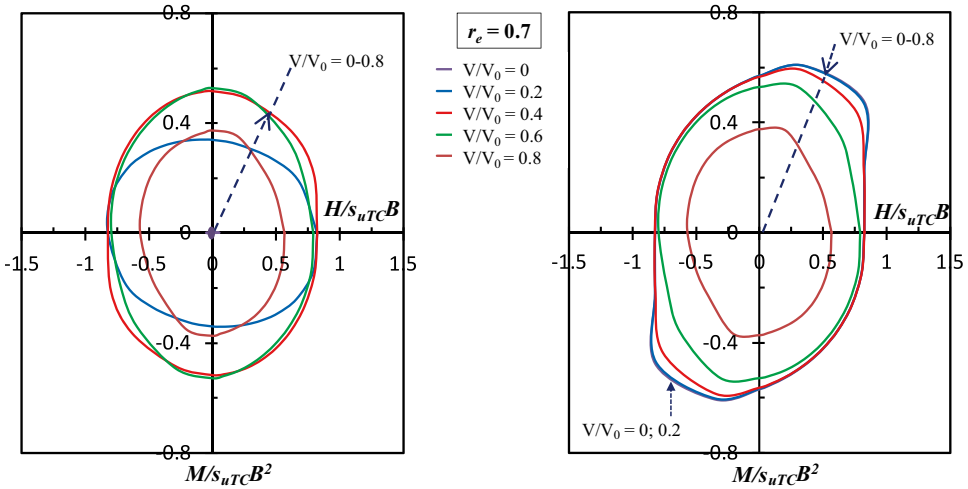

(a) No tension **(b)** Full tension

Fig. 12 Failure envelopes of strip footings with $r_e = 0.7$

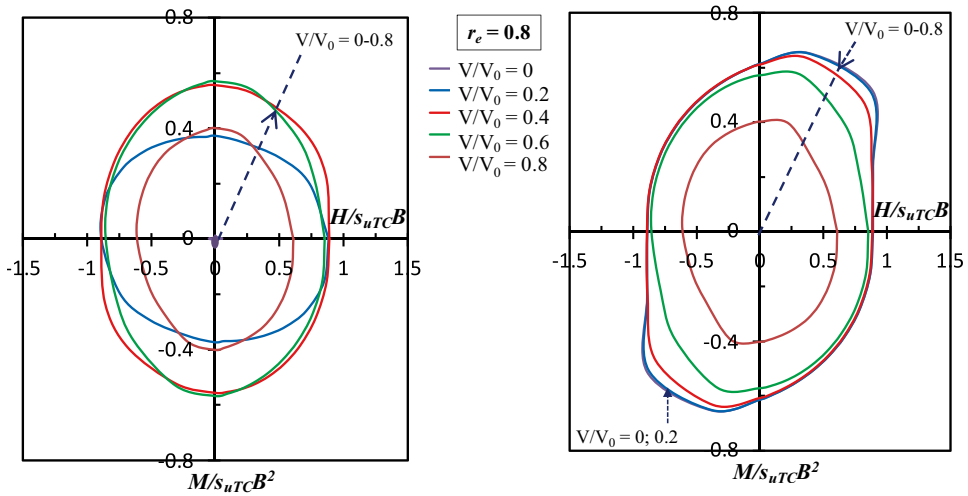

(a) No tension **(b)** Full tension

Fig. 13 Failure envelopes of strip footings with $r_e = 0.8$

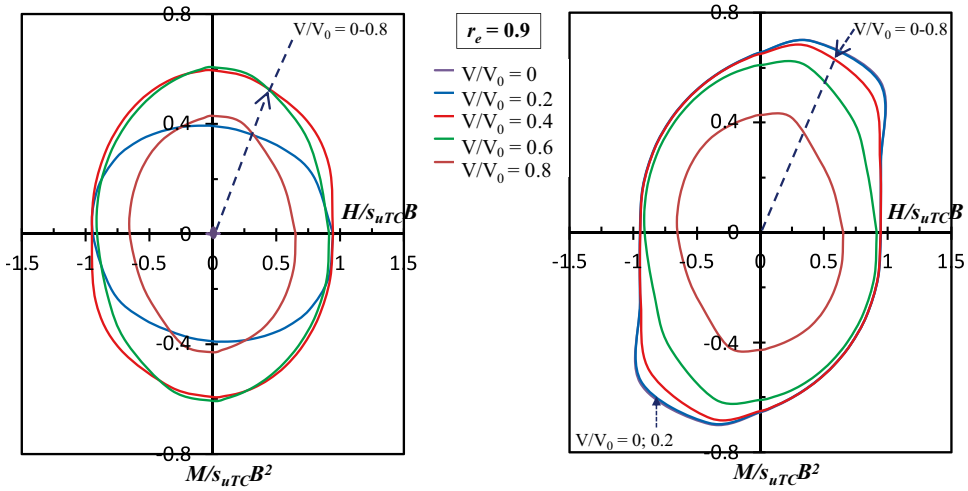

(a) No tension **(b)** Full tension

Fig. 14 Failure envelopes of strip footings with $r_e = 0.9$

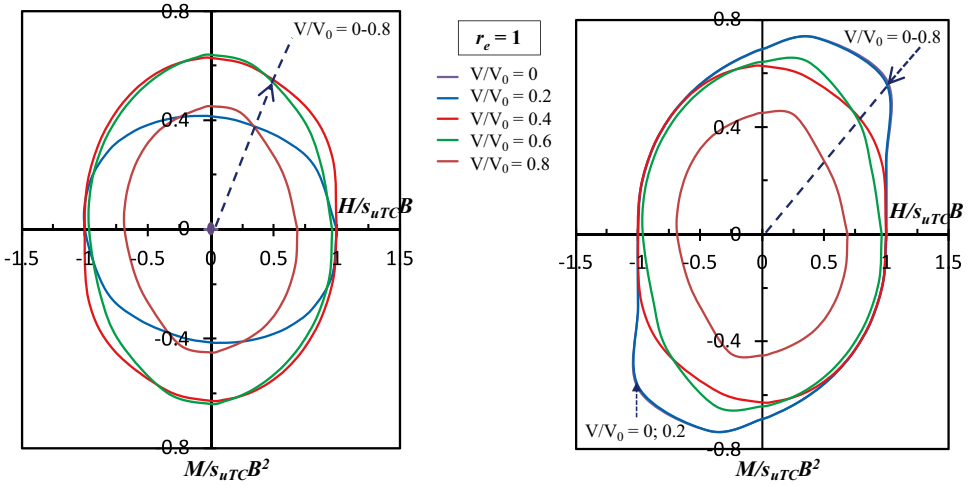

(a) No tension **(b)** Full tension

Fig. 15 Failure envelopes of strip footings with $r_e = 1$

of asymmetry influenced by the loadings combination and anisotropic strength ratios (r_e). As shown in Figs. 10, 11, 12, 13, 14 and 15 for cases of r_e [0.5, 0.6, 0.7, 0.8, 0.9, 1], the magnitude of the failure envelopes is significantly impacted by the values of r_e. An increase in r_e results in an increase in the size of the failure envelope. An increase in (r_e) leads to a greater obliqueness of the failure envelopes. In both interface conditions (full-tension and no-tension), the appearance of the envelopes for the different values of r_e is in a similar pattern. For full-tension cases, the case of $V/V_0 = 0$ expresses the largest *H-M* failure envelope for all values of r_e. Note that the contour dimensions are similar in both $V/V_0 = 0$ and 0.2 for the case of full-tension conditions. Moreover, as the normalized vertical load component (V/V_0) increases, the horizontal-moment capacity decreases, resulting in the failure envelope contracting towards the origin. On the contrary, in cases of no-tension interface, the size of the failure envelope for the case of $V/V_0 = 0$ is smallest and located at the origin point (0,0) because the footing cannot withstand any lateral force induced from *H* and *M* loadings owing to the soil-footing interface having zero tensile stress. However, in cases of no-tension interface when the value of V/V_0 increases, the size of the failure envelope becomes bigger since the applied vertical force can enhance the capacity at the connection between the footing and underlying clay.

Figures 16a, b illustrate the 3D failure envelopes (V/V_0, $H/s_{uTC}B$, $M/s_{uTC}B^2$) under two conditions: no-tension and full-tension, respectively. In this 3D diagram, the *x*-axis, *y*-axis, and *z*-axis represent the non-dimensional load variables of $H/s_{uTC}B$, $M/s_{uTC}B^2$, and V/V_0, respectively. The 3D failure envelope in no-tension and full-tension cases generally takes the form of an ellipsoid rotating along the vertical axis, arising from the favorable $H/s_{uTC}B$. The asymmetry arises due to the physical fact that combinations of

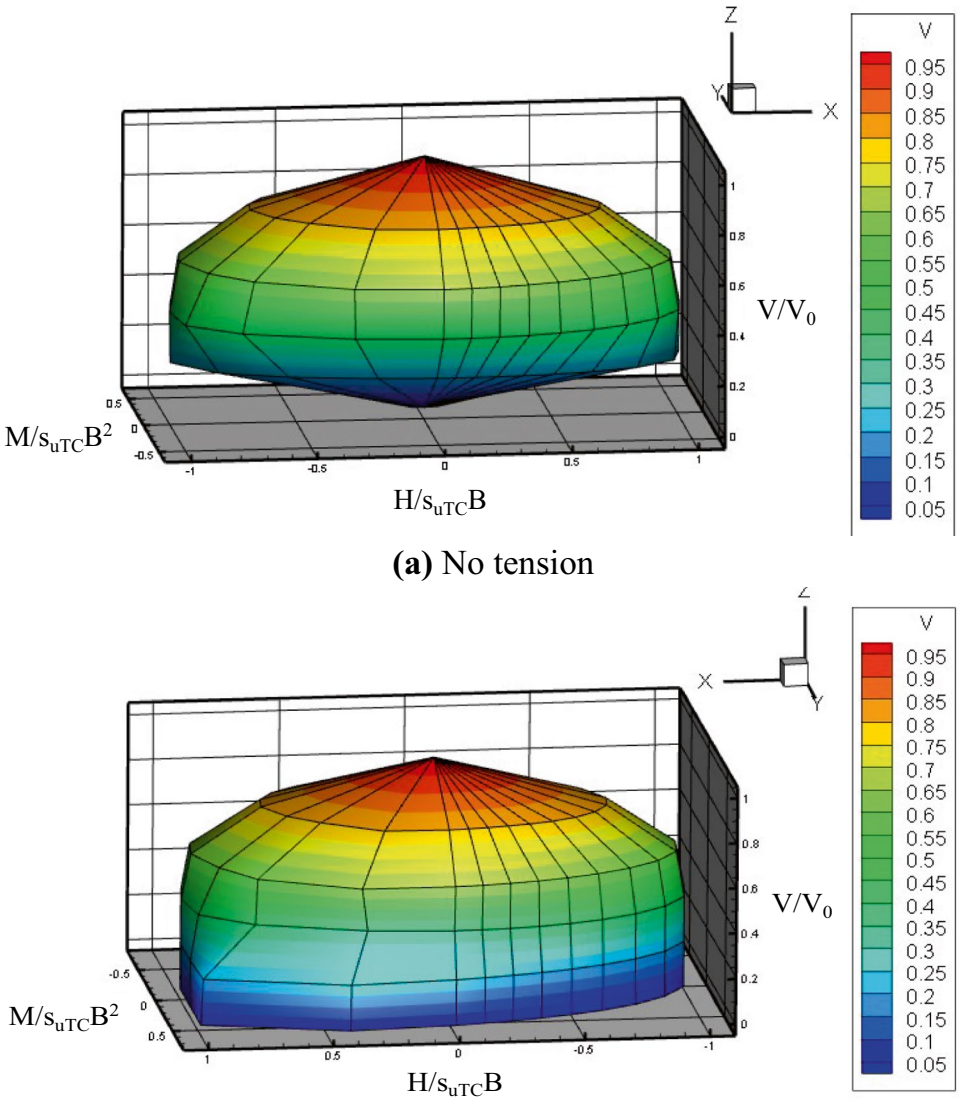

Fig. 16 Examples of 3D failure envelopes

horizontal and moment loads acting in the same direction are not equivalent to those acting in opposition. The diagram lacks symmetry when $V/s_{uTC}B = 0$.

In the upper part of the 3D failure envelopes where V/V_0 is larger than 0.6, the case with full-tension interaction is larger than the one with no-tension interaction. In the lower part of the 3D failure envelopes where value of V/V_0 is less than 0.6. For the no-tension case, it is found that the size of the cross-section of the failure envelope diminishes when the value of V/V_0 becomes zero. Without any tensile resistance or vertical load ($V/V_0 = 0$), the strip foundation would fail when subjected to a moment at low vertical loads, resulting in a diminished foundation capacity. Furthermore, the size of the 3D envelope of the full-tension case is much bigger and more asymmetric than another no-tension case when the value of V/V_0 is less than 0.6. The reason for these problems can be explained through the failure mechanism, as illustrated in Figs. 17 and 18.

The deformation patterns at failure obtained from FELA solutions with "no-tension" and "full-tension" conditions for the cases of $r_e = 0.5$ and 1 are shown in Figs. 17 and 18, respectively. It can be found in Figs. 17 and 18 that a combined sliding and rotating mechanism governs the failure. As shown in Fig. 17, for the no-tension cases, the separation between the footing and clay is recorded. In this case, the moment component increases (resulting in a decrease in horizontal capacity), and the sliding mechanism transitions into a shallow scoop for both $r_e = 0.5$ and 1. It can be explained that, in no-tension cases, the failure pattern is primarily driven by the impact of moment rather than the horizontal

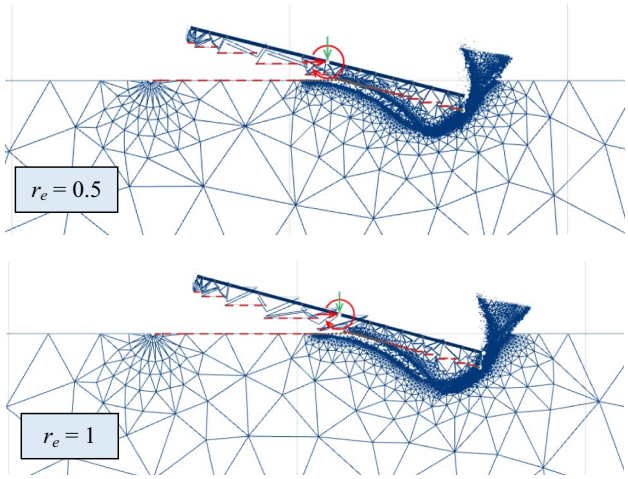

Fig. 17 Failure patterns of strip footings with no-tension interface, where $V/V_0 = 0.4$

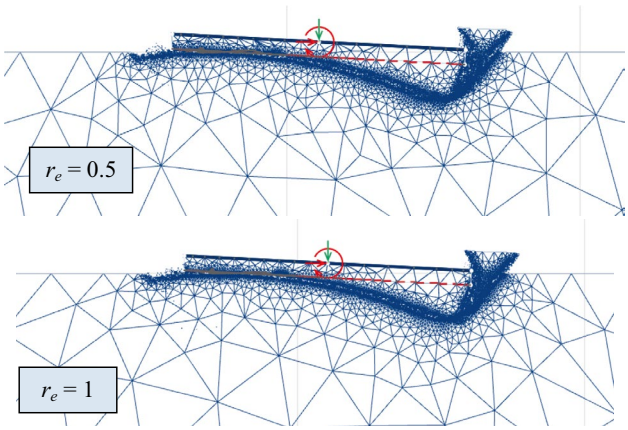

Fig. 18 Failure patterns of strip footings with full-tension interface, where $V/V_0 = 0.4$

force. This phenomenon results in a scoop-wedge mechanism, with the scoop component gaining greater significance as the moment increases. As shown in Fig. 18, since the interface between the clay and the footing is considered under the full-tension condition, there is no separation even though the footing is subjected to a sizeable horizontal load and moment. A non-symmetric wedge mechanism can be seen in Fig. 18. On other sides, it is noted that the anisotropic ratio (r_e) has a small impact on the failure patterns, as shown in Figs. 17 and 18.

To enhance the understanding of the failure mechanisms of this problem, a comparison of failure mechanisms under varying combinations of horizontal load and bending moment is shown in Fig. 19 for cases of full-tension interface. In that, the incremental deviatoric strain contours are used to express the failure patterns. Seven cases are examined, corresponding to different values of β angles, including $\beta = 0°$, 30°, 90°, 110°, 140°, 170°, and 180°. The failure mechanism is resulted from a combination of rotational and translational modes. The modes of horizontal displacements and rotations are created by applying the horizontal force and bending moment. The failure condition is generally associated with the sliding slip surface beneath the foundation, which behaves mostly like a scoop mechanism. In the first quadrant, where the (β) angle ranges from 0° to 90°, the maximum moment capacity is achieved since both horizontal load and moment are applied on the footing in the same direction. The plastic zone expands as (β) approaches 90°, leading to a wedge-scoop-wedge mechanism. This differs from the scoop-wedge mechanism noticed in the second quarter (with β ranging from 90° to 180°), where the directions of horizontal force and bending moment are different. It is noteworthy that the extent of the plastic zone diminished until (β) reached 180°, at which point the failure mechanism at $\beta = 180°$ became indistinguishable from that at $\beta = 0°$. The optimal mechanisms for $H/s_{uTC}B$ values just below or above $M/s_{uTC}B^2$ lead to backward (reverse to H) and forward foundation translation in addition to rotation.

ANN results

To select the optimal ANN model, in this study, the performance functions for feedforward networks are mean square error (MSE) and the coefficient of determination (R^2) between the network outputs and the target outputs. As shown in Fig. 20 for full-tension cases, the number of neurons is varied from 1 to 11 to investigate the impact of a number of neurons on the value of MSE and R^2. It should be noted that lower MSE values are better, and R^2 close to 1 means a close relationship. As a result, the optimal selection for the full-tension conditions uses 8 neurons in the hidden layer for the ANN architecture with the MSE and R^2 equal to 0.0006 and 0.9988, respectively. It means that the optimal ANN architecture utilized to predict the dimensionless horizontal load ($H/s_{uTC}B$) and bending moment ratio ($M/s_{uTC}B^2$) of the investigated strip footing on anisotropic clay are 3-8-2 (three input, eight hidden, and two output neurons). The analysis process will be carried out similarly in the cases of no-tension, as shown in Fig. 21. The optimal ANN model for cases of no-tension is also 3-8-2. After the updating weighs and bias in the training process, these optimal Neural Networks Constants values are shown in Tables 2 and 3.

The neural networks constants could be used to create the correlation equation between the three input variables (r_e, V/V_0, β) and the two outputs ($H/s_{uTC}B$, $M/s_{uTC}B^2$). As a short description, the correlation equation can be expressed

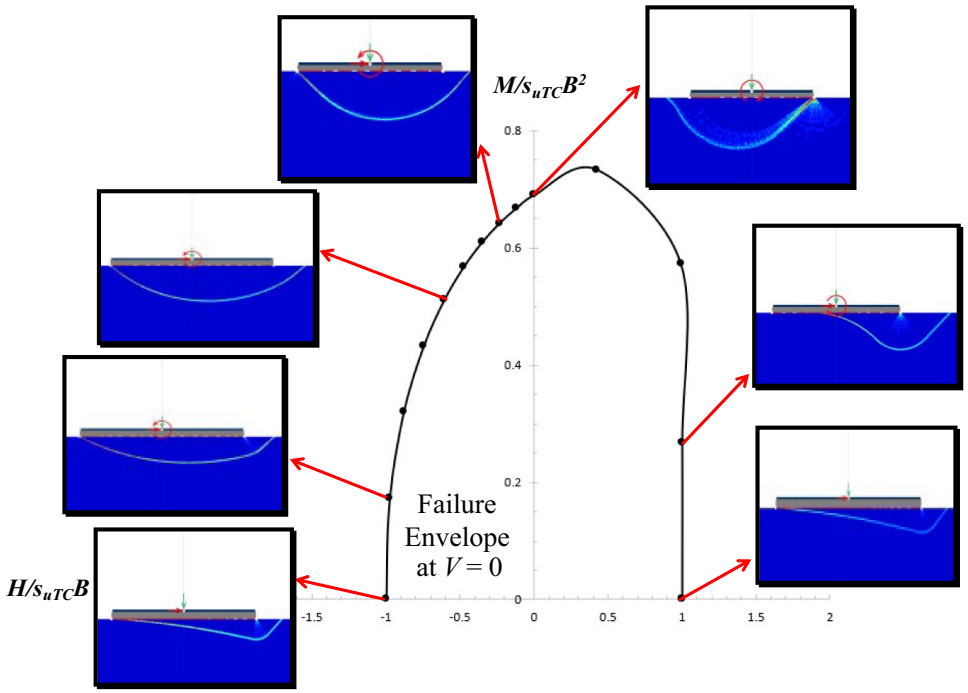

Fig. 19 Examples of failure mechanisms along the surface of a 2D failure envelop of a strip footing under general loading

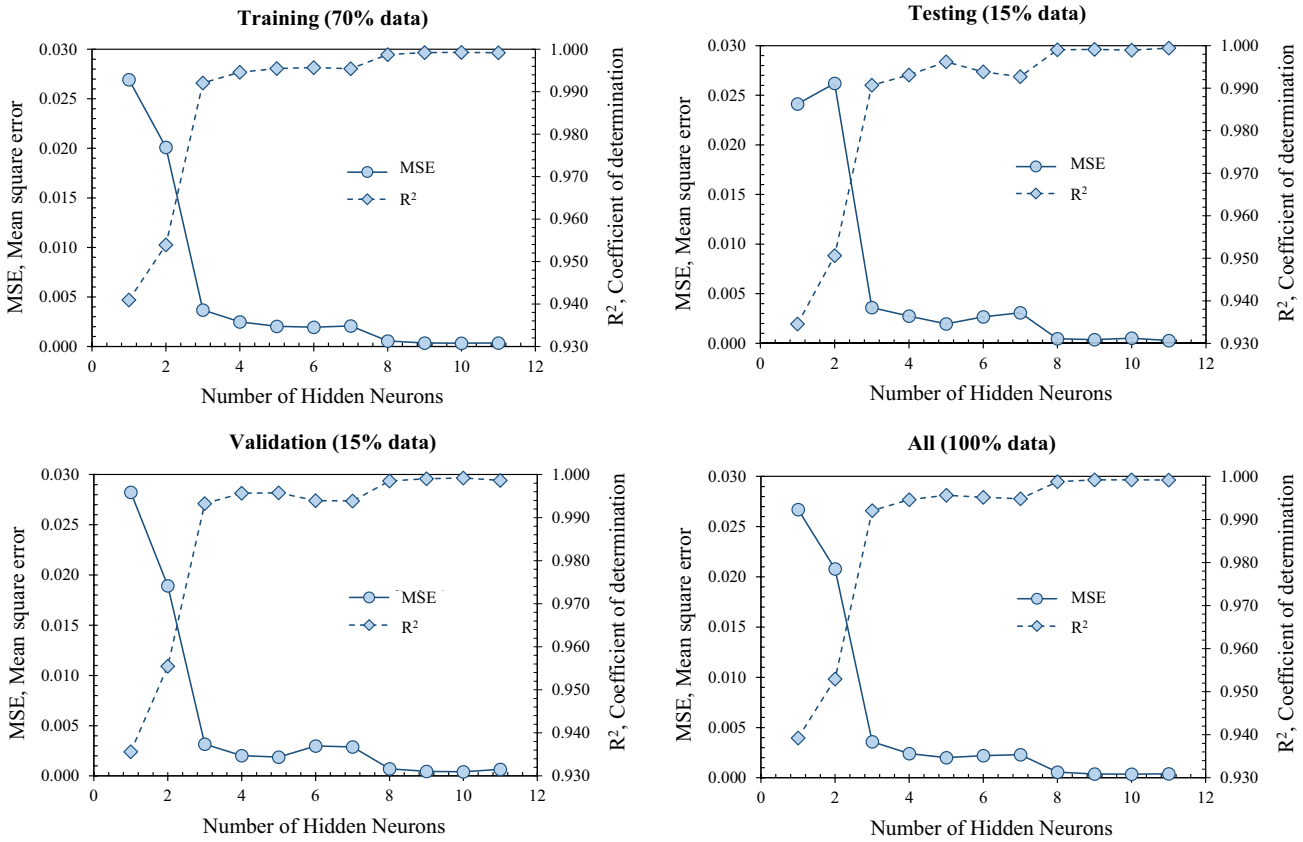

Fig. 20 The Mean Square Error (MSE) and Coefficient of determination (R^2) of the number of selected hidden neurons for full-tension cases

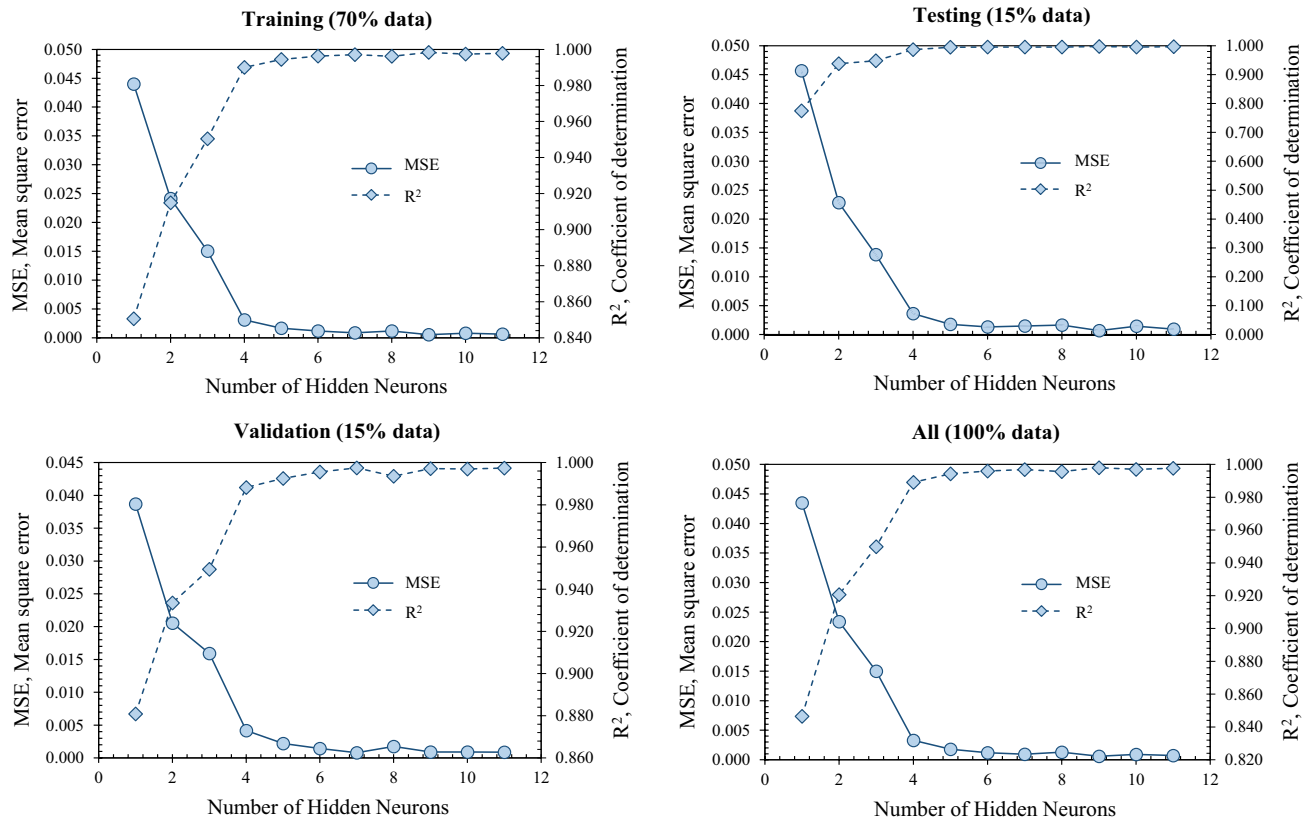

Fig. 21 The Mean Square Error (MSE) and Coefficient of determination (R^2) of the number of selected hidden neurons for no-tension cases

Table 2 Weights and Bias of the ANN model for full-tension cases

Neuron	W^{12}			b^{12}	W^{23}		b^{23}	
	Input variables				Output			
	r_e	V/V_0	β		$H/s_{uTC}B$	$M/s_{uTC}B^2$		
1	0.1797	1.9045	1.0338	− 2.7454	0.5397	0.1665	− 1.1005	− 6.2164
2	0.1110	0.0156	0.6109	− 1.1192	− 5.1610	− 2.2676		
3	− 0.0370	0.2793	− 0.0609	0.1564	− 4.2810	− 8.6456		
4	− 0.0467	0.8478	4.0437	2.4346	− 0.1956	− 0.3536		
5	0.0201	0.6080	− 0.0225	0.2852	2.1402	3.9972		
6	0.1289	− 0.1028	− 3.4743	− 3.0350	1.4163	− 3.9180		
7	0.0676	− 0.0838	1.6644	− 2.5432	2.1471	− 4.0740		
8	− 0.1151	0.0591	4.2550	3.6564	1.3008	− 2.2507		

through the hyperbolic tangent sigmoid (Tansig) function as shown in Eq. (6).

$$y_n = \left[\sum_{h=1}^{Nh} W^{23} tansig\left(\sum_{i=1}^{n}\left\{W^{12}x_{Ni}\right\} + b^1\right) + b^2\right] \quad (6)$$

where y_n is normalized output, W^{12} and W^{23} are the weight matrices value in hidden layer with tansigmoid and output layer with linear transfer function, b^1 and b^2 are the bias matrices in hidden and output layer, respectively, x_{Ni} are the normalized input values in the range $(h_{min}, h_{max}) = (-1,1)$ and is calculated in Eq. (7); N_i and N_h are the number of input and hidden neurons.

$$x_{Ni} = \frac{x_i - x_{min-i}}{x_{max-i} - x_{min-i}}\left(h_{max} - h_{min}\right) + h_{min} \quad (7)$$

Table3 Weights and Bias of the ANN model for no-tension cases

Neuron	W^{12}			b^{12}	W^{23}		b^{23}	
	Input variables				Output			
	r_e	V/V_0	β		$H/s_{uTC}B$	$M/s_{uTC}B^2$		
1	− 0.1113	1.3186	0.8764	− 1.9487	0.5434	1.4619	1.9494	− 5.9733
2	− 0.0354	0.5096	1.2221	− 1.2101	− 0.5360	− 6.3716		
3	0.0609	− 0.8485	0.4135	− 0.7521	− 4.9188	− 0.7339		
4	0.1039	0.5186	0.4006	0.8191	2.8575	0.1561		
5	− 0.0217	0.7081	0.4908	0.4999	− 2.9650	1.6990		
6	− 0.0306	− 0.2940	− 2.2199	1.4255	0.2433	− 2.1190		
7	− 0.0054	− 0.6041	0.4395	− 1.0194	7.0870	− 2.0440		
8	0.1035	− 0.7711	1.1624	1.1374	− 0.3559	2.1609		

The ANN prediction is determined by Eq. (8), which is the reverse normalizing of the normalized values of input and output variables of training data.

$$y = \left(y_n - h_{min}\right)\frac{\left(y_{0-max} - y_{0-min}\right)}{\left(h_{max} - h_{min}\right)} + y_{0-min} \tag{8}$$

To be more precise and applicable for practical engineering, the detailed calculation described below shows an example of calculating the predicted value of ($H/s_{uTC}B$, $M/s_{uTC}B^2$) in the case of ($r_e = 0.5$, $V/V_0 = 0$, $\beta = 0$), with full-tension condition. The simple three steps include:

1. The normalized values for three input variables (r_e, V/V_0, β), $x_{Ni} = (-1, -0.5, -0.8333)$ are given by Eq. (7).

2. Substitute the value of x_{Ni} into the formulas following Eq. (6) below.

$$N_1 = tansig\left(0.1791r_e + 1.9045V/V_0 + 1.0338\beta - 2.7454\right) = -0.9998$$

$$N_2 = tansig\left(0.1110r_e + 0.0156V/V_0 + 0.6109\beta - 1.1192\right) = -0.9410$$

$$N_3 = tansig\left(-0.0370r_e + 0.2793V/V_0 - 0.0609\beta + 0.1564\right) = 0.1042$$

$$N_4 = tansig\left(-0.0467r_e + 0.8478V/V_0 + 4.0437\beta + 2.4346\right) = -0.8649$$

$$N_5 = tansig\left(0.0201r_e + 0.6080V/V_0 - 0.0225\beta + 0.2852\right) = -0.0200$$

$$N_6 = tansig\left(0.1289r_e - 0.1028V/V_0 - 3.4743\beta - 3.0350\right) = -0.2139$$

$$N_7 = tansig\left(0.0676r_e - 0.0838V/V_0 + 1.6644\beta - 2.5432\right) = -0.9993$$

$$N_8 = tansig\left(-0.1151r_e + 0.0591V/V_0 + 4.2550\beta + 3.6564\right) = 0.1936$$

$$H/s_{uTC}B = 0.5397N_1 - 5.1610N_2 - 4.2810N_3 - 0.1956N_4 + 2.1402N_5 + 1.4163N_6 + 2.1471N_7 + 1.3008N_8 - 1.1005 = 0.7003$$

$$M/s_{uTC}B^2 = 0.1665N_1 - 2.2676N_2 - 8.6456N_3 - 0.3536N_4 + 3.9972N_5 - 3.9180N_6 - 4.0740N_7 - 2.2507N_8 - 6.2164 = -0.4504$$

3. The predicted value in the instance of ($r_e = 0.5$, $V/V_0 = 0$, $\beta = 0$) is given by Eq. (8).

(A) For $H/s_{uTC}B$

$$y = \left(y_n - h_{min}\right)\frac{\left(y_{0-max} - y_{0-min}\right)}{\left(h_{max} - h_{min}\right)} + y_{0-min} = 0.7003$$

(B) For $M/s_{uTC}B^2$

$$y = \left(y_n - h_{min}\right)\frac{\left(y_{0-max} - y_{0-min}\right)}{\left(h_{max} - h_{min}\right)} + y_{0-min} = 0.2020$$

FELA results for the case of ($r_e = 0.5$, $V/V_0 = 0$, $\beta = 0$) with ($H/s_{uTC}B$, $M/s_{uTC}B^2$) = (0.6665, 0.1786) where ANN prediction is (0.7003, 0.2020). The error between the ANN prediction and the FELA results is less than 12.00%.

According to the above calculation, all predictions for both full-tension and no-tension cases from the ANN model are compared with FELA results, as shown in Figs. 22 and 23, respectively. The prediction results agreed with the FELA results, with MSE and R^2 values of (0.0006, 99.88%) and (0.00013, 99.57%) for full-tension and no-tension conditions, respectively. As a result, the suggested equation can be utilized confidently to calculate dimensionless horizontal force ($H/s_{uTC}B$) and bending moment ($M/s_{uTC}B^2$) of the strip footing on anisotropic clay under combined loading. It should be noted that the prediction may be inaccurate if the parameter input value is out of training data.

Design example

As reference practical instruction for practitioners in applying ANN results to establish 2D and 3D failure envelopes of a strip footing on anisotropic clay under general loading (*V*-*H*-*M*), the paper presents a practical example, as follows:

A strip footing on clay characterized by anisotropic soil behavior has to be designed to determine the failure envelope under combined loading. The strip foundation measuring $B=2$ m in width lies on the surface of anisotropic clay. The interface condition between the clay and foundation is supposed to be "full-tension". It is given that $r_e=0.6$, $s_{uTC}=50$ kPa. Assume that β is from 0° to 180°, $V/V_0=0.2$, and V_0 is defined as a function of r_e, presented in Table 4.

From Table 4, it can be noted that the value of $V_0/s_{uTC}B$ becomes equal to 3.838 since $r_e=0.6$. On substituting the value of B and s_{uTC}, it can be seen that $V_0=383.8$ kN and $V=76.76$ kN. Let $r_e=0.6$, $V/V_0=0.2$. For $\beta=30°$, the values of the factors $H/s_{uTC}B$ and $M/s_{uTC}B^2$, using Eqs. (6–8), are 0.4276 and 0.2469, respectively. Therefore, the design will provide the value of $H=42.76$ kN and $M=49.38$ kNm in the full-tension condition. Similarly, a sequence of investigations is conducted by altering β angles to obtain the corresponding lateral and bending moment loads. According to this procedure, a graph depicting the relationship between H and M is produced as shown in Fig. 24. Furthermore, by varying the V/V_0 from 0 to 1, the 3D failure envelope of strip footing on anisotropic clay for case ($B=2$, $s_{uTC}=50$ kPa, $r_e=0.6$) can be established, as shown in Fig. 25.

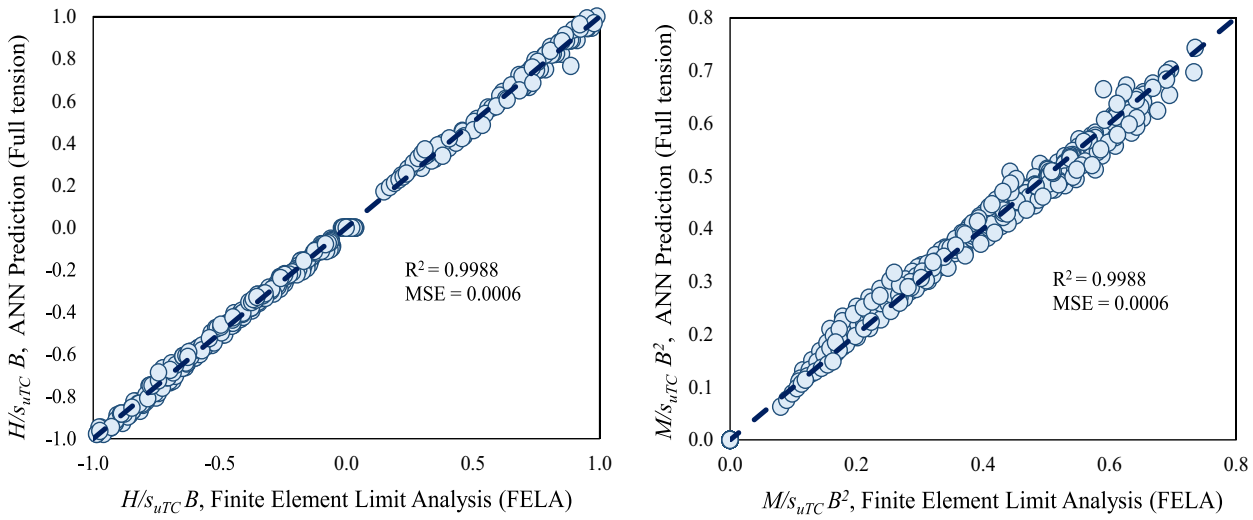

Fig. 22 The comparison between the results of ANN predictions and FELA results for the full-tension cases

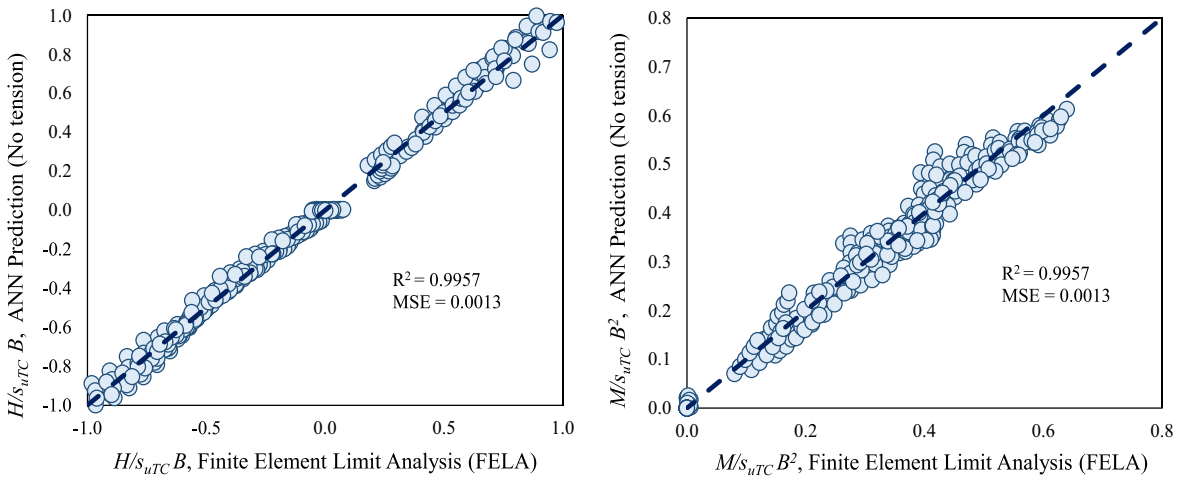

Fig. 23 The comparison between the results of ANN predictions and FELA results for the no-tension cases

Table 4 Summary of vertical ultimate load $V_0/s_{uTC}B$ for strip foundation in anisotropic clay

Anisotropic ratio (r_e)	0.5	0.6	0.7	0.8	0.9	1
Vertical ultimate load ($V_0/s_{uTC}B$)	3.41	3.838	4.213	4.552	4.85	5.122

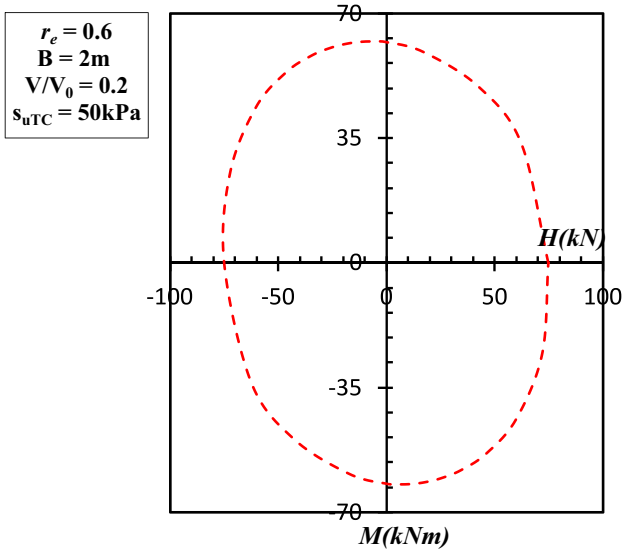

Fig. 24 2D failure envelope in (*H, M*) plane for the case of $V/V_0 = 0.2$, $B = 2$ m, $s_{uTC} = 50$ kPa, and $r_e = 0.6$

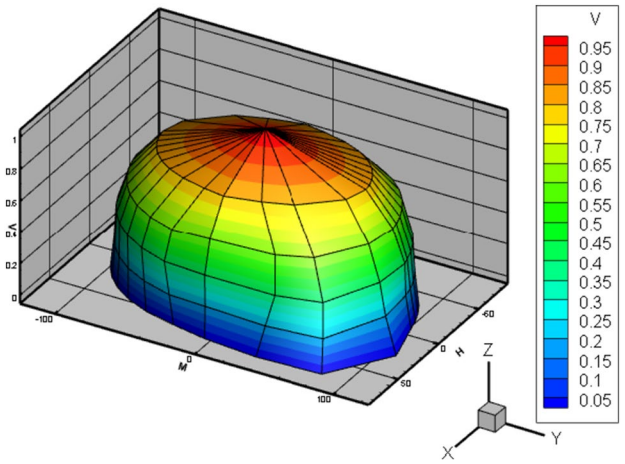

Fig. 25 3D failure envelope for the case of $B = 2$, $s_{uTC} = 50$ kPa, and $r_e = 0.6$

Conclusions

The paper studied the failure envelopes of strip footing in anisotropic clay under general loading (*V-H-M*) by applying the lower bound solutions of 2D FELA and artificial neuron networks (ANN). The results of the paper are summarized as follows:

1. The effect of the anisotropic behavior of clay on the bearing capacity of the investigated strip footing under general loading (*V-H-M*) is carefully investigated through the 2D failure envelope ($H/s_{uTC}B$, $M/s_{uTC}B^2$) at various cross-sections ($V/V_0 = 0$, 0.2, 0.4, 0.6, 0.8) of the 3D failure envelope (V/V_0, $H/s_{uTC}B$, $M/s_{uTC}B^2$). As a result, an increase in (r_e) makes the 2D failure envelope bigger, but does not affect much on the change of the shape of the failure envelope.
2. The impacts of the interface interaction between soil and footing are investigated through 2D and 3D failure envelopes and failure mechanisms. The results show that the shapes of the 3D failure envelopes between no-tension and full-tension cases are different. In the upper part of the 3D failure envelope where V/V_0 is larger than 0.6, 3D failure envelopes in full-tension cases are larger than those in no-tension cases. The reason can be found through the failure mechanism of the investigated strip footing where the soil and footing are separated due to the setting of no-tension conditions at the interface of soil and footing. In the lower part of the 3D failure envelope where V/V_0 is less than 0.6, the shapes of 3D failure envelopes seem to be likely symmetry in no-tension cases and asymmetry in full-tension cases.
3. The ANN model is applied in this study to propose an efficient tool for practical engineering to build 2D space ($H/s_{uTC}B$, $M/s_{uTC}B^2$) and 3D failure envelope (V/V_0, $H/s_{uTC}B$, $M/s_{uTC}B^2$. In detail, the correlation equations are proposed to show the relationship between ($H/s_{uTC}B$, $M/s_{uTC}B^2$) and (r_e, V/V_0, β). As a result, with the instance value of the input design parameter, i.e., (r_e, B, s_{uTC}), the 2D failure envelope ($H/s_{uTC}B$, $M/s_{uTC}B^2$) and 3D failure envelope (V/V_0, $H/s_{uTC}B$, $M/s_{uTC}B^2$) can establish quickly and high accuracy. As reference practical instruction, a practical example with careful explanations is presented for practitioners.

Acknowledgements We acknowledge Ho Chi Minh City University of Technology (HCMUT), VNU-HCM for supporting this study.

Author contributions DTT: Investigation, Software, Writing- Original draft preparation, Visualization, Validation, Writing-Reviewing and Editing. MNT: Investigation, Software, Writing- Original draft preparation, Visualization, Validation, Writing-Reviewing and Editing. VQL: Conceptualization, Methodology, Supervision, Data curation, Visualization, Investigation, Software, Validation, Writing- Original draft preparation, Writing- Reviewing and Editing. SK: Conceptualization,

Methodology, Supervision, Data curation, Visualization, Investigation, Investigation, Software, Validation, Writing- Reviewing and Editing.

Data availability The datasets used and/or analysed during the current study are available from the corresponding author upon reasonable request.

Declarations

Conflict of interest The authors declare that they have no conflict of interest with this work. We declare that there are no commercial or associative interests that represent a conflict of interest in connection with the work submitted.

Ethical approval This article does not contain any studies with human participants or animals performed by any of the authors.

References

Abdollahi F, Hosseini S, Sabet M, Esmaeili-Faraj SM, Amiri F (2021) A novel study of the gas lift process using an integrated production/injection system using artificial neural network approach. Model Earth Syst Environ 7:2101–2112

Ahmad F, Hussain A, Ansari MA (2022) Development of ANN model for the prediction of discharge coefficient of an arced labyrinth side weir. Model Earth Syst Environ 9:1835–1842

Beale MH, Hagan MT, Demuth HB (2010) Neural network toolbox 7. User's Guide, MathWorks, 2

Bolton MD, Lau CK (1993) Vertical bearing capacity factors for circular and strip footings on mohr-coulomb soil. Can Geotech J 30:1024–1033

Bransby MF, Randolph MF (1998) Combined loading of skirted foundations. Géotechnique 48(5):637–655

Bransby MF, Yun GJ (2009) The undrained capacity of skirted strip foundations under combined loading. Géotechnique 59(2):115–125

Brinch Hansen J (1970) A revised and extended formula for bearing capacity. Dan Geotech Inst Bull 28:5–11

Butterfield R (1999) Dimensional analysis for geotechnical engineering. Géotechnique 49(2):357–366

Butterfield R, Gottardi G (1994) A complete three-dimensional failure envelope for shallow footings on sand (technical note). Géotechnique 44(1):181–184

Butterfield R, Ticof J (1979) Design parameters for granular soils (discussion contribution). In: Proc. 7th European Conf. on Soil Mech. and Foundation Eng, Brighton, 4:259–261

Cherif K, Yahia N, Bilal B (2023) Erosion potential model-based ANN-MLP for the spatiotemporal modeling of soil erosion in wadi Saida watershed. Model Earth Syst Environ 9:3095–3117

Das BM, Larbi-Cherif S (1983) Bearing capacity of two closely-spaced shallow foundations on sand. Soil Found 23:1–7

Davis EH, Christian JT (1971) Bearing capacity of anisotropic cohesive soil. J Soil Mech Found Div 97(5):753–769

Feng X, Randolp MF, Gourvenec S, Wallerand R (2014) Design approach for rectangular mudmats under fully three-dimensional loading. Géotechnique 64(1):51–63

Gottardi G, Butterfield R (1993) On the bearing capacity of surface footings on sand under general planar load. Soils Found 33(3):68–79

Gourvenec S (2007) Failure envelopes for offshore shallow foundations under general loading. Geotechnique 57:715–728

Gourvenec S (2008) Effect of embedment on the undrained capacity of shallow foundations under general loading. Geotechnique 58(3):177–185

Gourvenec S, Barnett S (2011) Undrained failure envelope for skirted foundations under general loading. Géotechnique 61(3):263–270

Gourvenec SM, Randolph MR (2003) Effect of strength non-homogeneity on the shape and failure envelopes for combined loading of strip and circular foundations on clay. Géotechnique 53(6):575–586

Hagan MT, Menhaj MB (1994) Training feedforward networks with the Marquardt algorithm. IEEE Trans Neural Netw 5(6):989–993

Houlsby GT, Puzrin AM (1999) The bearing capacity of a strip footing on clay under combined loading. Proc R Soc Lond Ser A 455:893–916

Ibrahim AS, Musa AA, Abdulfatah AY, Idris A (2022) Developing soft-computing regression model for predicting soil bearing capacity using soil index properties. Model Earth Syst Environ 9:1223–1232

Kapadia D, Jariwala N (2021) Prediction of tropospheric ozone using artificial neural network (ANN) and feature selection techniques. Model Earth Syst Environ 8:2183–2192

Keawsawasvong S, Ukritchon B (2016) Three-dimensional interaction diagram for the undrained capacity of inverted T-shape strip footings under general loading. Int J Geotech Eng 12(2):133–146

Krabbenhoft K, Lyamin A, Krabbenhoft J (2015) Optum computational engineering (OptumG2). www.optumce.com

Krabbenhoft K, Galindo-Torres SA, Zhang X, Krabbenhoft J (2019) AUS: Anisotropic undrained shear strength model for clays. Int J Numer Anal Meth Geomech 43(17):2652–2666

Kumar J, Ghosh P (2007) Ultimate bearing capacity of two interfering rough strip footings. Int J Geomech 7:53–62

Kumar M, Kumar V, Rajagopal BG, Samui P, Burman A (2023b) State of art soft computing based simulation models for bearing capacity of pile foundation: a comparative study of hybrid ANNs and conventional models. Model Earth Syst Environ 9:2533–2551

Kumar A, Chauhan VB, Kumar P (2023a) Integration of AFELA and machine learning for analysis of shallow foundation over horseshoe tunnel in rock mass. Model Earth Syst Environ

Ladd CC, DeGroot DJ (2003) Recommended practice for soft ground site characterization. Arthur Casagrande Lecture. In: Proceedings of the 12th Panamerican Conference on soil mechanics and geotechnical engineering, Cambridge

Lai VQ, Shiau J, Promwichai T, Limkatanyu S, Banyong R, Keawsawasvong S (2023) Modelling soil stability in wide tunnels using FELA and multivariate adaptive regression splines analysis. Model Earth Syst Environ 9:2993–3008

Law KT (1978) Undrained strength anisotropy in embankment stability analysis. Can Geotech J 15(2):306–309

Mana DKS, Gourvenec S, Martin CM (2013) Critical skirt spacing for shallow foundations under general loading. ASCE J Geotech Geoenviron Eng 139(9):1554–1566

Martin CM (1994) Physical and numerical modelling of offshore foundations under combined loads. DPhil thesis, University of Oxford, UK

Martin CM, Houlsby GT (2000) Combined loading of spudcan foundations on clay: Laboratory tests. Geotechnique 50:325–338

Martin CM, Houlsby GT (2001) Combined loading of spudcan foundations on clay: numerical modelling. Géotechnique 51(8):687–699

Meyerhof GG (1953) The bearing capacity of foundations under eccentric and inclined loads. In: Proc 3rd Int. Conf. Soil Mech. Found. Engng, Zurich, 1: 440–445

Nova R, Montrasio L (1991) Settlements of shallow foundations on sand. Géotechnique 41(2):243–256

Pan Q, Dias D (2016) Face stability analysis for a shield-driven tunnel in anisotropic and nonhomogeneous soils by the kinematical approach. Int J Geomech 6(3):04015076

Reddy AS, Rao KV (1981) Bearing capacity of strip footing on anisotropic and nonhomogeneous clays. Soils Found 21(1):1–6

Roscoe KH, Schofield AN (1957) The stability of short pier foundations in sand: discussion. Br Weld J, pp 12–18

Saint-Fleur BE, Allier S, Lassara E (2023) Towards a better consideration of rainfall and hydrological spatial features by a deep neural network model to improve flash floods forecasting: case study on the Gardon basin. France Model Earth Syst Environ 9:3693–3708

Salencon J, Peeker A (1995) Ultimate bearing capacity of shallow foundations under inclined and eccentric loads. Part I: purely cohesive soil. Eur J Mech A/Solids 14(3):349–375

Shams SR, Jahani A, Moeinaddini M, Khorasani N (2020) Air carbon monoxide forecasting using an artificial neural network in comparison with multiple regression. Model Earth Syst Environ 6:1467–1475

Sloan SW (2013) Geotechnical stability analysis. Géotechnique 63(7):531–572

Su SF, Liao HJ, Lin YH (1998) Base stability of deep excavation in anisotropic soft clay. J Geotech Geoenviron Eng 124(9):809–819

Taiebat HA, Carter JP (2000) Numerical studies of the bearing capacity of shallow foundations on cohesive soil subjected to combined loading. Géotechnique 50(4):409–418

Taiebat HA, Carter JP (2002) Bearing capacity of strip and circular foundations on undrained clay subjected to eccentric loads. Géotechnique 52(1):61–64

Ukritchon B, Whittle AJ, Sloan SW (1998) Undrained limit analysis for combined loading of strip footings on clay. J Geotech Geoenviron Eng ASCE 124(3):265–276

Ukritchon B, Whittle AJ, Sloan SW (2003) Undrained stability of braced excavations in clay. J Geotech Geoenviron Eng 129(8):738–755

Vesic AS (1975) Bearing capacity of shallow foundations. In: Winterkorn HF, Fang HY (eds) Foundation engineering handbook. Van Nostrand, New York, pp 121–147

Vulpe C, Bienen B, Gaudin C (2013) Predicting the undrained capacity of skirted spudcans under combined loading. Ocean Eng 74:178–188

Yang XL, Du DC (2016) Upper bound analysis for bearing capacity of nonhomogeneous and anisotropic clay foundation. KSCE J Civ Eng 20(7):2702–2710

Yun G, Bransby MF (2007) The horizontal-moment capacity of embedded foundations in undrained soil. Can Geotech J 44(4):409–424

Zhang Y, Bienen B, Cassidy MJ, Gourvenec S (2011) The undrained bearing capacity of a spudcan foundation under combined loading in soft clay. Mar Struct 24(4):459–477

Publisher's Note Springer Nature remains neutral with regard to jurisdictional claims in published maps and institutional affiliations.

Springer Nature or its licensor (e.g. a society or other partner) holds exclusive rights to this article under a publishing agreement with the author(s) or other rightsholder(s); author self-archiving of the accepted manuscript version of this article is solely governed by the terms of such publishing agreement and applicable law.